The onset of fabric development in deep marine sediments

Maffione, Marco; Morris, Antony

[Link to publication on Research at Birmingham portal](#)

Highlights
- High-resolution AMS study of deep marine clay-rich sediments from IODP Site U1438
- Compaction-related fabrics initiate sharply at 83 mbsf (5.7 Ma after deposition)
- Fabrics continue to form over a 6 Ma long, 30 m thick 'initial compaction window'
- An effective stress threshold triggers compaction-related fabric development

1   **The onset of fabric development in deep marine sediments**

2   Marco Maffione[1,2] and Antony Morris[3]

3   [1]School of Geography, Earth and Environmental Sciences, University of

4   Birmingham, Edgbaston, Birmingham, B15 2TT, UK

5   [2]Department of Earth Sciences, Utrecht University, Heidelberglaan 2, 3584 CS

6   Utrecht, Netherlands

7   [3]School of Geography, Earth and Environmental Sciences, Plymouth University,

8   Drake Circus, Plymouth, PL4 8AA, UK

9

10

14

15   **Abstract**

16   Post-depositional compaction is a key stage in the formation of sedimentary

17   rocks that results in porosity reduction, grain realignment and the production of

18   sedimentary fabrics. The progressive time-depth evolution of the onset of fabric

19   development in deep marine sediments is poorly constrained due to the limited

20   quantity and resolution of existing data. Here we present high-resolution

21   anisotropy of magnetic susceptibility (AMS) results from clay-rich deep marine

22   sediments recovered at International Ocean Discovery Program Site U1438

23   (Philippine Sea). AMS is a petrofabric tool sensitive to the preferred orientation

24   of grains in rocks. Down-section variations of AMS parameters, density, porosity

25   and the inclination of magnetic remanences demonstrate that fabrics develop in

26   response to compaction and dewatering but also that they do not develop

27   progressively with depth below the mudline. Instead, a horizontal foliation first

28   forms at 83 mbsf once the sediment load reaches an effective stress threshold for

29   the onset of compaction and is then continuously enhanced down to 113 mbsf,

30   defining a 30 m-thick 'initial compaction window'. The magnetostratigraphic age

31   model for IODP Site U1438 indicates a delay of 5.7 Ma in initial fabric formation

32   following sediment deposition, with strongly defined fabrics then taking an

33   additional 6.5 Ma to develop.

34

35   **1. Introduction**

36   During deposition of (hemi)pelagic sediments in deep-sea environments, platy

37   minerals (mainly phyllosilicates) tend to align with their long axes parallel to the

38   water-sediment interface. Bottom-current disturbance and bioturbation,

39   together with the natural predisposition of clay flakes to form edge-to-edge and

40   edge-to-face contacts due to surface electric charge distribution (Bennett et al.,

41   1991), eventually result in an uppermost sedimentary interval characterized by

42   a chaotic internal structure (i.e., isotropic fabric) and high porosity and water

43   content (Bennett et al., 1991; Reynolds and Gorsline, 1992). With increasing

44   vertical burial load at depth, clays particles rotate to form horizontal face-to-face

45   contacts, accompanied by simultaneous dewatering and porosity reduction

46   (Bennett et al., 1981; Bennett and Hulbert, 1986). The effect of this process on

47   the microstructure of the sediment is the formation of a fabric characterized by a

48   well-defined horizontal foliation plane.

49   The majority of dewatering and compaction in pelagic sedimentary sequences is

50   thought to occur progressively within the uppermost stratigraphic intervals (e.g.,

51   Arason and Levi, 1990). However, only a few previous studies have investigated

52   microstructure changes during compaction and initial fabric development in

53   deep marine environments (Kopf and Behrmann, 1997; Hirano et al., 2001;

54   Kawamura and Ogawa, 2002; 2004), and none have a sufficiently high spatial

55   and temporal resolution to describe in detail the evolution of this process.

56   Here we present results of a high-resolution anisotropy of magnetic

57   susceptibility (AMS) analysis of a sequence of unconsolidated deep marine

58   sediments recovered in the Philippine Sea by International Ocean Discovery

59   Program (IODP) Expedition 351 (Arculus et al., 2015a), where

60   magnetostratigraphy provides an accurate age model. We use AMS as a sensitive

61   measure of fabric development in these sediments (e.g., Rochette et al., 1992;

62   Tarling and Hrouda, 1993; Borradaile and Jackson, 2004), and compare magnetic

63   fabric parameters with other physical properties to tightly constrain the depth

64   and timing of the onset and evolution of fabric development in a deep marine

65   environment.

66

67   **2. Geological background and sampling**

68   *2.1. Tectonic framework of the Philippine Sea Plate and IODP Site U1438*

69   The Philippine Sea Plate (PSP) is an oceanic plate located between the Eurasia

70   and Pacific plates and bordered by active subduction zones (Figure 1). The PSP

71   can be subdivided into three tectono-stratigraphic domains: (i) a western

72   domain floored by a complex array of oceanic plateaux, ridges, and basins of

73   Cretaceous to Oligocene age and bordered to the east by the Eo-Oligocene (~55-

74   25 Ma) Kyushu-Palau Ridge (e.g., Deschamps and Lallemand, 2003; Okino and

75   Fuijoka, 2003; Ishizuka et al., 2011a, 2013); (ii) a central domain dominated by

76   the Miocene (~25-12 Ma) Parece Vela-Shikoku back-arc basin (Okino et al.,

77   1994) occurring between the Kyushu-Palau Ridge and the modern Izu-Bonin-

78   Mariana (IBM) arc; and (iii) an eastern domain forming the forearc region

79   between the modern IBM arc and the IBM trench, developed upon initiation of

80   subduction of the Pacific plate below the PSP at ~52 Ma (Ishizuka et al., 2011b;

81   Reagan et al., 2010; Arculus et al., 2015b).

82   During June and July 2014, IODP Expedition 351 (Arculus et al., 2015a)

83   recovered a suite of sedimentary and volcanic rocks at Site U1438 (4700 m

84   water depth) in the western domain of the PSP (Amami Sankaku Basin; 27.38°N,

85   134.32°E; Figure 1a). Four progressively deeper holes were drilled at this site,

86   down to 26.5, 257.3, 897.8, and 1611 metres below seafloor (mbsf), at Holes

87   U1438A, B, D and E respectively. Recovered rocks (Figure 1b) consist of a thick

88   sedimentary sequence (Units I-IV) deposited since the Early Eocene (~55 Ma)

89   and recording the birth, evolution and death of the Kyushu-Palau Ridge,

90   overlying igneous basement rocks (Unit 1).

91

92   *2.2. Deep marine sedimentation in the west PSP (Unit I)*

93   Unit I (0-160.3 mbsf; Hole U1438B) is an unconsolidated fine-grained pelagic

94   and hemipelagic sedimentary sequence composed of mud, tuffaceous mud, mud

95   with ash, and clay with discrete ash beds. Paleomagnetic and biostratigraphic

96   constraints place the base of Unit I at the Miocene-Oligocene transition (Arculus

97   et al., 2015a). Deposition of Unit I therefore started soon after the demise of

98   Kyushu-Palau Ridge volcanism and initial opening of the Parece Vela-Shikoku

99   back-arc basin to the east (thought to occur at ~25 Ma; Okino et al., 1994). Since

100   no significant tectonic events occurred since that time at the location of Site

101   U1438, Unit I represents the product of deep marine sedimentation, with

102   sedimentation rates ranging from ~2 to ~0.5 cm/kyr (Arculus et al., 2015a).

103   The average grain size of Unit I changes slightly down-core, with the uppermost

104   interval (0-45 mbsf) mainly represented by siltstones with a significant (up to

105   60%) biogenic, mainly siliceous component, a central interval (45-93 mbsf)

106   dominated by claystones with a lower biogenic content, and a bottom interval

107   (93-160.3 mbsf) represented again predominantly by siltstones. Bioturbation is

108   rare in the upper interval of Unit I (< 93 mbsf) and increases at depth, with more

109   bioturbated intervals occurring below 121 mbsf. X-Ray diffraction analyses

110   revealed a predominant assemblage of quartz, plagioclase, chlorite, muscovite,

111   illite and other clay minerals (Arculus et al., 2015a). Below ~93 mbsf (in the

112   lower siltstones) quartz content decreases, while the content of zeolite and clay

113   minerals increases.

114

115   **3. Methods**

116   Anisotropy of magnetic susceptibility (AMS) is a petrofabric tool used to

117   determine the preferred orientation of minerals (e.g., Jelínek, 1981; Hrouda,

118   1982; Borradaile, 1988; Rochette et al., 1992; Tarling and Hrouda, 1993;

119   Borradaile and Jackson, 2004). AMS is geometrically described by an ellipsoid

120   with principal axes corresponding to the minimum (k_{min}), intermediate (k_{int}), and

121   maximum (k_{max}) susceptibilities (Hrouda, 1982). The relative magnitude of the

122   susceptibility axes defines the shape of the AMS ellipsoid, which can be: (1)

123   isotropic ($k_{min} = k_{int} = k_{max}$) when grains are not aligned preferentially; (2) oblate

124   ($k_{min} << k_{int} \approx k_{max}$) when grain alignment defines a foliation plane; (3) triaxial

125   ($k_{min} < k_{int} < k_{max}$) when grain alignment results in a well-defined foliation and a

126   lineation; or (4) prolate ($k_{min} \approx k_{int} << k_{max}$) when grain alignment defines a

127   lineation. Here we describe the strength of anisotropy using the corrected

128   anisotropy degree (P_J; Jelínek,1978), where P_J = 1.0 indicates an isotropic fabric

129   and, e.g., P_J = 1.05 indicates 5% anisotropy. The shape of the ellipsoid is

130   described by the shape parameter (T), where -1.0 < T < 1.0 and positive/negative

131   values of T indicate oblate/prolate fabrics respectively (Jelínek 1978).

132   Sedimentary fabrics are characterised by P_J > 1.0, oblate AMS ellipsoids (0 < T <

133   1), vertical k_{min} axes, and k_{int} and k_{max} axes dispersed within the horizontal

134   foliation plane.

135   We measured the anisotropy of low-field magnetic susceptibility of 173 discrete,

136   8 cm^3 cubic samples from the top 140 m of Unit I. Measurements were carried

137   out using an AGICO KLY-3S Kappabridge (Plymouth University), and

138   susceptibility tensors and associated eigenvectors and eigenvalues calculated

139   using AGICO Anisoft 4.2 software. Instrument precision for AMS measurements

140   for the KLY-3S system is > 99%, yielding meaningful principal directions in

141   weakly anisotropic rocks when P_J > 1.003 (Burmeister et al., 2009). Sample

142   orientations were determined by correcting cores recovered from Hole U1438B

143   to the geographic reference frame using "FlexIT" tool data obtained during

144   advanced piston corer (APC) deployments (Arculus et al., 2015a).

145   Rock magnetic experiments were performed to investigate the nature of the

146   mineral fractions contributing to the AMS. Curie temperatures were determined

147   from the high-temperature (20-700°C) variation of magnetic susceptibility of

148   representative samples, measured using a KLY-3S coupled with a CS-3 high-

149   temperature furnace apparatus. Isothermal remanent magnetization (IRM)

150   acquisition experiments were conducted on representative samples using a

151   Molspin pulse magnetizer to apply peak fields up to 800 mT with resulting IRMs

152   measured using an AGICO JR6A spinner magnetometer.

153   Finally, we also employ shipboard paleomagnetic and physical property data

154   from Hole U1438B, collected using methods documented in Arculus et al.

155   (2015a).

156

157   **4. Results**

158   AMS parameters from the investigated interval of Unit I are extremely variable

159   with depth, with a clear change occurring at 83 mbsf (Figure 2; Supplementary

160   material Table 1). The anisotropy degree is low ($P_J \approx 1.006$) indicating weakly

161   anisotropic sediments in the uppermost 83 m of the sequence, but progressively

162   increases over an interval of ~30 m below 83 mbsf, reaching a maximum of P_J

163   ≈ 1.060 at 113 mbsf (Figure 2a). Similarly the shape parameter (T) is extremely

164   variable from -1.0 to +1.0 in the upper interval, becoming consistently oblate

165   (0.6 < T < 1.0) immediately below 83 mbsf, and then strongly oblate (0.8 < T <

166   1.0) below 113 mbsf (Figure 2b). In addition, the orientation of the principal

167   susceptibility axes changes with depth. Above 83 mbsf, magnetic fabrics are

168   randomly oriented, with only the k_{min} axes showing a faint alignment near the

169   vertical (Figure 3a). Below 83 mbsf, k_{min} axes become tightly clustered along the

170   vertical, and the k_{int} and k_{max} axes align with the horizontal plane (Figure 3b). A

171   weak clustering of k_{max} axes along an ESE-NWN orientation is also observed,

172   potentially reflecting weak bottom water currents during deposition (Hrouda

173 and Jezek, 1999). Mean magnetic susceptibility shows a slight increase with

174 depth from ∼30 to ∼80 x 10^{-5} SI (Figure 2c).

175 Results from high-temperature variation of magnetic susceptibility experiments

176 revealed consistent maximum Curie temperatures of ∼580°C (Figure 4a),

177 indicating that the ferromagnetic fraction in these sediments is dominated by

178 near-stoichiometric magnetite (Dunlop and Özdemir, 1997). This is consistent

179 with IRM acquisition experiments, where saturation was reached at applied

180 fields of 200-300 mT (Figure 4b), consistent with the presence of low-coercivity,

181 fine-grained (single-domain to pseudo-single-domain) magnetite. However, the

182 vertical alignment of k_{min} axes (perpendicular to horizontal bedding in the

183 sediments) indicates a dominance of normal sedimentary fabrics, and excludes

184 the presence of significant inverse magnetic fabric components due to single

185 domain effects in these sediments (Potter and Stephenson, 1988).

186

187 **5. Discussion**

188 *5.1. Comparison of AMS fabric variations with physical properties*

189 Interpretation of AMS data requires understanding of the source of the

190 susceptibility signal and its potential variability downhole. A linear relationship

191 between low field magnetic susceptibility and the intensity of natural remanent

192 magnetization (NRM) suggests constancy of ferromagnetic mineralogy and

193 grain-size (domain state) through Unit I (Figure 4c), implying that the

194 contribution of magnetite to the susceptibility signal is controlled by

195 concentration alone. The relatively low bulk magnetic susceptibility (Figure 2c),

196 however, indicates that magnetite content is low and that the paramagnetic

197 phyllosilicate matrix is likely the main contributor to susceptibility in these

198   sediments, as typically observed in clay-rich sediments (e.g., Borradaile and

199   Jackson, 2004; Sagnotti and Speranza, 1993; Maffione et al., 2012, 2015; Parés,

200   2015).

201   The rapid increase of the anisotropy degree, together with the acquisition of a

202   consistently oblate fabric below 83 mbsf within Unit I (Figure 2) marks the onset

203   of development of a horizontal foliation typical of sedimentary fabrics (Figure

204   3b). This foliation is progressively enhanced down to 113 mbsf, where the

205   anisotropy degree reaches a maximum and AMS ellipsoids become strongly

206   oblate (Figure 2b). This depth interval of fabric development coincides with a

207   distinct decrease in porosity from 75 to 65% and increase in bulk density from

208   ~1.45 to ~1.55 g/cm^3 (Figure 2d), seen in shipboard physical property data

209   acquired on discrete samples analysed during IODP Expedition 351 (Arculus et

210   al., 2015a). This suggests that fabrics have developed in response to mechanical

211   compaction and dewatering occurring during burial diagenesis due to increasing

212   effective overburden stress. Chemical compaction is considered insignificant in

213   Unit I, as this generally only becomes a significant porosity-occluding process at

214   depths greater than ~2 km (Bjørlykke and Høeg, 1997; Mondol et al., 2008). An

215   apparent increase in sedimentation rate from ~0.5 to ~2.0 cm/ka at 83 mbsf

216   (Figure 2e) is likely to also result from mechanical compaction rather than a

217   change in rate of sediment supply.

218

219   *5.2. Paleomagnetic evidence for compaction*

220   As an additional test for the compaction-related origin of fabric development we

221   analyzed the occurrence of inclination shallowing of paleomagnetic remanences,

222   which characteristically results from compaction (e.g., Anson and Kodama, 1987;

223   Arason and Levi, 1990; Tauxe and Kent, 2004; Huang et al., 2013). Shipboard

224   remanence directions are presented in Figure 5 (based on measurements of

225   archive half core sections following alternating field demagnetization at 25 mT to

226   remove significant drilling-induced components; Figure 6). Inclinations above 83

227   mbsf are close to the value expected at IODP Site U1438, but are generally

228   shallower than expected below this (Figure 5a). To test this statistically, we

229   selected only data from the bottom 1.0 m of each core in order to exclude

230   intervals affected by drilling-induced shearing (commonly encountered in IODP

231   piston cores (Acton et al., 2002) and evident in the declination data of Figure 5b).

232   Mean inclinations were calculated after transposing all data to normal polarity

233   and applying a fixed 45° cut-off to the distribution of corresponding virtual

234   geomagnetic poles (following the methodology of Johnson et al. (2008)). For the

235   uppermost 83 m of Unit I, the mean inclination of 44.1° (α_{95} = 1.2°, n = 408) is

236   not statistically different from the expected geocentric axial dipole (GAD)

237   inclination at this site (I = 46°). In contrast, the mean inclination below 83 mbsf

238   (I = 39.7°; α_{95} = 1.8°, n = 266) is statistically significantly shallower. Using the

239   elongation/inclination (E/I) correction method (Tauxe and Kent, 2004) we

240   obtained an unflattened inclination for the interval 83-140 mbsf of 42.8° (95%

241   confidence limits: 40.2°-53.4°) consistent with the expected inclination. These

242   results further confirm that mechanical compaction has affected the lower

243   interval of Unit I but is absent or not statistically significant at shallower depths.

244

245   *5.3. Potential causes of the sudden onset of fabric development at 83 mbsf*

246   *5.3.1. Comparison with compaction trends for marine mudrocks*

247 Effective stress-controlled mechanical compaction at the relative shallow depths

248 of Unit I in Hole U1438B might be expected to produce continuous changes in

249 physical properties, i.e. with a progressive decrease in porosity and increase in

250 anisotropy degree with depth. Following Kopf and Behrmann (1997), we

251 compare downhole porosity variations with published mechanical compaction

252 functions by converting porosity determinations to uniaxial vertical shortening

253 values, e_v using:

$$e_v = \frac{P_0 - P}{P - 100}$$

254 where P is a given sample porosity (in %) and P_0 is an initial porosity near the

255 mudline (taken as 75%). Figure 7 compares the resulting values to converted

256 porosity-depth trends for clays and claystones of Terzaghi (1925), Athy (1930),

257 Hamilton (1976) and Sclater and Christie (1980). Though variable, each model

258 predicts a smooth, monotonic increase in shortening with depth, in contrast to

259 the stepwise increase at 83 mbsf in Unit I from e_v values close to zero (mean = -

260 0.03) to a mean value of -0.21 below. This is consistent with the AMS data that

261 show a uniformly low anisotropy degree down to 83 mbsf and then a sharp

262 change in character to pronouncedly oblate fabrics. Hence, factors other than

263 continuous compaction across the whole depth interval of Unit I must influence

264 fabric development in these sediments.

265

266 *5.3.2. Apparent overconsolidation*

267 The sharp increase of the anisotropy degree in the studied unit resembles the

268 pattern expected for "apparent overconsolidation" (Schwehr et al., 2006),

269 whereby sediments appear more consolidated than predicted by simple burial

270   for a given depth. According to Schwehr et al. (2006) apparent overconsolidation

271   can result from unconformities produced by underwater landslides, which

272   unload pre-consolidated sediments that then become buried by new sediments.

273   Alternatively, overconsolidation can be caused by repeated shaking events

274   (Locat and Lee, 2002). The continuous magnetostratigraphic record at Unit I

275   (Arculus et al., 2015a), however, excludes the existence of unconformities within

276   the sequence, and it is unlikely that seismic events only caused

277   overconsolidation of the interval of Unit I below 83 mbsf without also affecting

278   the top of the section in this tectonically active region.

279

280   *5.3.3. Compositional control*

281   Compaction of sediments can be controlled by variations in the composition and

282   size of sedimentary grains, with, for example, platy hyllosilicate minerals tending

283   to facilitate compaction. However, no major change in phyllosilicate mineralogy,

284   grain size or degree of bioturbation of the mudrocks of Unit I (Arculus et al.,

285   2015a) corresponds with the sharp onset of fabric development at 83 mbsf.

286   Curtis et al. (1980) have demonstrated that although preferred orientations in

287   clay-rich sediments commonly result from compactional strain, fabric

288   development may be affected by the presence of non-platy silicate particles

289   (such as quartz grains) which inhibit planar fabric development in their

290   immediate vicinity. In this context, we note a downhole decrease in the volume

291   percentage of fine-grained quartz particles in the mudrocks, from an average of

292   8% to 4% (based on smear-slide data collected during shipboard analyses;

293   Arculus et al., 2015a). This minor compositional change is illustrated semi-

294   quantitatively by variations in the intensity of quartz peaks at 26.6° 2θ in XRD

295   analyses of Unit I mud samples (Figure 2g; data from Arculus et al., 2015a).

296   Quartz content, however, mainly decreases between 50 and 65 mbsf (Figure 2g),

297   and remains constant throughout the interval where sharp variations of AMS

298   parameters are observed. Furthermore, the volume percentage change in quartz

299   affecting fabric development in the mudrocks analysed by Curtis et al. (1980)

300   was much more dramatic (28% to 15%). Finally, the combined volume

301   percentage of the main non-platy silicates (quartz plus feldspar) in Hole U1438B

302   increases slightly from 12% to 15% across the interval where AMS fabrics

303   develop (Arculus et al., 2015a), suggesting that this mechanism cannot account

304   for the stepwise change in anisotropy observed here.

305

306   *5.3.4. An effective stress threshold for the 'initial compaction window'*

307   The stepwise variation of anisotropy parameters, porosity/vertical shortening

308   and bulk density with depth documented here suggests that compaction and

309   sedimentary fabric development is not progressive, but only starts once the

310   burial load produces a sufficient effective stress to exceed the internal resistance

311   to compaction represented by the friction along grain contacts during

312   reorientation. In this case, the density data of Figure 2d, a water depth of 4700 m

313   and a seawater density of 1029 kg/m^3 combine to yield an effective stress at 83

314   mbsf of 0.35 MPa (where effective stress = total stress – pore water pressure

315   (assumed to be hydrostatic); Terzaghi, 1925). Sedimentary fabric in the studied

316   section then develops over a restricted interval between 83 and 113 mbsf here

317   defined as the 'initial compaction window', where pore reduction and preferred

318   horizontal alignment of phyllosilicate flakes is progressively enhanced over a 30

319   m-thick interval. A similar compaction window can also be inferred in pelagic

320   sediments from ODP Site 1149 in the NW Pacific Ocean, where a stepwise change

321   in physical properties occurs between 118 and 150 mbsf (Kawamura and Ogawa,

322   2002; 2004).

323

324   *5.4 Implications for fabric studies on deformed ancient mudrocks*

325   The excellent age control at Site U1438, based on the IODP Expedition 351

326   shipboard magnetostratigraphy that successfully identified every geomagnetic

327   chron in core sections back to 36 Ma (Arculus et al., 2015a), provides constraints

328   on the timing of initial development of sedimentary fabrics in Unit I mudrocks.

329   These indicate that the full process of fabric development documented here

330   started 5.7 Ma after initial deposition and then took 6.5 Ma to complete (Figure

331   2e). This has implications for studies using AMS to document the progressive

332   tectonic overprinting of sedimentary fabrics in ancient mudrocks (e.g., Sagnotti

333   et al., 1998; Larrasoaña et al., 2004). Such studies typically assume that initial

334   sedimentary fabrics (which are subsequently partially overprinted by tectonic

335   fabrics) correspond to the biostratigraphic age of the sampled rocks. Instead

336   results here suggest that a ~6 Ma hiatus between deposition and initial fabric

337   development may need to be considered when documenting the evolution of

338   anisotropy in deep marine mudrocks.

339

340   **6. Conclusions**

341   A detailed record of progressive fabric development in deep marine sediments

342   sampled at IODP Site U1438 with robust age control indicates that a compaction-

343   related horizontal foliation started to form 5.7 Ma after initial sedimentation (83

344   mbsf) and developed over the subsequent 6.5 Ma (down to 113 mbsf), within a

345 30 m-thick interval here termed the 'initial compaction window'. These new

346 results provide the first high-resolution time/depth constraints on the onset of

347 fabric development in deep marine environments, with implications for the

348 tectonic application of AMS in pelagic sedimentary rocks. More data are now

349 required from such deep marine environments to determine the variability in

350 the onset of the initial compaction window, including additional quantification of

351 clay microfabrics through this window using scanning electron microscope

352 (SEM) and transmission electron microscope (TEM) techniques.

353

366

367 **References**

368 Acton, G. D., 2002. Paleomagnetic overprints in ocean sediment cores and their
369   relationship to shear deformation caused by piston coring. J. Geophys. Res.
370   107, doi: 10.1029/2001JB000518.

371 Anson, G. L. and Kodama, K. P., 1987. Compaction-induced inclination shallowing
372   of the post-depositional remanent magnetization in a synthetic sediment.
373   Geophys. J. Int. 88, 673-692.
374 Arason, P. and Levi, S., 1990. Compaction and inclination shallowing in deep-sea
375   sediments from the Pacific Ocean, J. Geophys. Res., 95(B4), 4501-4510,
376   doi:10.1029/JB095iB04p04501.
377 Arculus, R. J., Ishizuka, O., Bogus, K. and the Expedition 351 Scientists, 2015a.
378   Proceedings of the International Ocean Discovery Program Volume 351,
379   doi:10.14379/iodp.proc.351.103.2015.
380 Arculus, R. J., Ishizuka, O., Bogus, K., Gurnis, M., Hickey-Vargas, R., Aljahdali, M. H.,
381   Bandini-Maeder, A. N., Barth, A. P., Brandl, P., Drab, L., do Monte Guerra, R.,
382   Hamada, M., Jiang, F., Kanayama, K., Kender, S., Kusano, Y., Li, H., Loudin, L.
383   C., Maffione, M., Marsaglia, K. M., McCarthy, A., Meffre, S., Morris, A., Neuhaus,
384   M., Savov, I. P., Sena, C., Tepley III, F. J., van der Land, C., Yogodzinski, G. M.
385   and Zhang, Z., 2015b. A record of spontaneous subduction initiation in the
386   Izu–Bonin–Mariana arc. Nat. Geosci. 8, 728–733, doi: 10.1038/ngeo2515.
387 Athy, L. F., 1930. Density, porosity and compaction of sedimentary rocks
388   (abstract). American Association of Petroleum Geologists, Bulletin, 14, 24.
389 Bennett, R. H., Bryant, W. R. and Keller, G. H., 1981. Clay fabric of selected
390   submarine sediments: fundamental properties and models. J. Sediment.
391   Petrol. 51, 217-232.
392 Bennett, R. H., O'Brien, N. R. and Hulbert, M. H., 1991. Determinants of clay and
393   shale microfabric signatures: processes and mechanisms. In: Bennett, R. H.,
394   Bryant, W. R. and Hulbert, M. H. (Eds.), Microstructures of Fine-grained
395   Sediments from Mud to Shale. Springer-Verlag, New York, pp. 5 –32.
396 Bennett, R. H. and Hulbert, M. H., 1986. Clay Microstructure. Boston
397   (International Human Resources Development Corp. Publ.).
398 Bjørlykke, K. and Høeg, K., 1997. Effects of burial diagenesis on stresses,
399   compaction and fluid flow in sedimentary basins. Marine and Petroleum
400   Geology, 14, 267-276.
401 Borradaile, G. J., 1988. Magnetic-susceptibility, petrofabrics and strain:
402   Tectonophysics 156, 1–20, doi: 10.1016/0040-1951(88)90279-x.
403 Borradaile, G. J. and Jackson, M., 2004. Anisotropy of magnetic susceptibility
404   (AMS): magnetic petrofabrics of deformed rocks. Geol. Soc. London Sp. Pub.
405   238, 299–360, doi: 10.1144/GSL.SP.2004.238.01.18.
406 Burmeister, K. C., Harrison, M. J., Marshak, S., Ferré, E. C., Bannister, R. A. and
407   Kodama, K. P., 2009. Comparison of Fry strain ellipse and AMS ellipsoid
408   trends to tectonic fabric trends in very low-strain sandstone of the
409   Appalachian fold–thrust belt. J. Struct. Geol. 31, 1028-1038.
410 Curtis, C. D., Lipshie, S. R., Oertel, G. and Pearson, M. J., 1980. Clay orientation in
411   some Upper Carboniferous mudrocks, its relationship to quartz content
412   and some inferences about fissility, porosity and compactional history.
413   Sedimentology 27, 333-339.
414 Deschamps, A. and Lallemand, S., 2003. Geodynamic setting of Izu-Bonin-
415   Mariana boninites. Geol. Soc. London Sp. Publ. 219, 163–185, doi:
416   10.1144/GSL.SP.2003.219.01.08.
417 Dunlop, D. J. and Özdemir, Ö., 1997. Rock magnetism: fundamentals and
418   frontiers. Cambridge University Press, Cambridge, 573 pp.
419 Hamilton, E. L., 1976. Variations of density and porosity with depth in deep sea

420 sediments. Journal of Sedimentary Petrology, 46, 280-300.

421 Hirano, S., Ogawa, Y. and Kawamura, K., 2001. Deformation of unlithified
422 sediments in an early stage of the compaction process deduced from
423 microtextures and magnetic fabrics: ODP Leg 174B, Hole 1074A. In: Becker,
424 K., Malone, M.J. (Eds.), Proc. ODPSci. Results, vol. 174B, 1 –13.

425 Hrouda, F., 1982. Magnetic anisotropy of rocks and its application in geology and
426 geophysics. Geophys. Surveys 5, 37–82, doi: 10.1007/BF01450244.

427 Hrouda, F. and Jezek, J., 1999. Magnetic anisotropy indications of deformations
428 associated with diagenesis. In: Tarling, D. H. and Turner, P. (eds),
429 Palaeomagnetism and Diagenesis in Sediments, Geological Society, London,
430 Special Publication, 151, 127-137.

431 Huang, W., Dupont-Nivet, G., Lippert, P. C., van Hinsbergen, D. J. J. and Hallot, E.,
432 2013. Inclination shallowing in the Eocene Linzizong sediments from Tibet:
433 correction, possible causes and implications for reconstructing the India-
434 Asia collision. Geophys. J. Int. 194, 1390-1411.

435 Ishizuka, O., Taylor, R. N., Yuasa, M. and Ohara, Y., 2011a. Making and breaking an
436 island arc: A new perspective from the Oligocene Kyushu-Palau arc,
437 Philippine Sea. Geochem. Geophys. Geosys. 12, 1–40, doi:
438 10.1029/2010GC003440.

439 Ishizuka, O., Tani, K., Reagan, M. K., Kanayama, K., Umino, S., Harigane, Y.,
440 Sakamoto, I., Miyajima, Y., Yuasa, M. and Dunkley, D. J., 2011b. The
441 timescales of subduction initiation and subsequent evolution of an oceanic
442 island arc. Earth Planet. Sci. Lett. 306, 229–240, doi:
443 10.1016/j.epsl.2011.04.006

444 Ishizuka, O., Taylor, R. N., Ohara, Y. and Yuasa, M. , 2013. Upwelling, rifting, and
445 age-progressive magmatism from the Oki-Daito mantle plume. Geology, 41,
446 1011–1014.

447 Jelínek, V., 1978. Statistical processing of anisotropy of magnetic susceptibility
448 measured on groups of specimens. Studia Geophys. Geod. 22, 50–62, doi:
449 10.1007/BF01613632.

450 Jelínek, V., 1981. Characterization of the magnetic fabric of rocks. Tectonophysics
451 79, 63-67.

452 Johnson, C. L., Constable, C. G., Tauxe, L., Barendregt, R., Brown, L. L., Coe, R. S.,
453 Layer, P., Mejia, V., Opdyke, N. D., Singer, B. S., Staudigel, H. and Stone, D. B.,
454 2008. Recent investigations of the 0-5 Ma geomagnetic field recorded by
455 lava flows. Geochemistry, Geophys. Geosystems, 9(4),
456 doi:10.1029/2007GC001696.

457 Kawamura, K. and Ogawa, Y., 2002. Progressive microfabric changes in
458 unconsolidated pelagic and hemipelagic sediments down to 180 mbsf,
459 northwest Pacific, ODP Leg 185, Site 1149. In Ludden, J.N., Plank, T., and
460 Escutia, C. (Eds.), Proc. ODP, Sci. Results, 185.

461 Kawamura, K. and Ogawa, Y., 2004. Progressive change of pelagic clay
462 microstructure during burial process: examples from piston cores and ODP
463 cores. Marine Geol. 207, 131-144. doi:10.1016/j.margeo.2004.03.016.

464 Kopf, A. and Behrmann, J. H., 1997. Fabric evolution and mechanisms of
465 diagenesis in fine-grained sediments from the Kita-Yamato Trough, Japan
466 Sea. J. Sedim. Res. 67, 590–600.

467 Larrasoaña, J. C., Pueyo, E. L. and Pares, J. M., 2004. An integrated AMS, structural,
468 palaeo- and rock-magnetic study of Eocene marine marls from the Jaca-

469   Pamplona basin (Pyrenees, N Spain); new insights into the timing of
470   magnetic fabric acquisition in weakly deformed mudrocks. Geol. Soc.
471   London Sp. Publ. 238, 127–143, doi: 10.1144/GSL.SP.2004.238.01.10.

472 Locat, J. and Lee, H., 2002. Submarine landslides: Advances and challenges.
473   Canadian Geotech. J. 39, 193–212.

474 Maffione, M., Pucci, S., Sagnotti, L. and Speranza, F., 2012. Magnetic fabric of
475   Pleistocene continental clays from the hanging-wall of an active low-angle
476   normal fault (Altotiberina Fault, Italy). Int. J. Earth Sci. 101, 849–861, doi:
477   10.1007/s00531-011-0704-9.

478 Maffione, M., Hernandez-Moreno, C., Ghiglione, M. C., Speranza, F., van
479   Hinsbergen, D. J. J. and Lodolo, E., 2015. Constraints on deformation of the
480   Southern Andes since the Cretaceous from anisotropy of magnetic
481   susceptibility. Tectonophysics 665, 236–250, doi:
482   10.1016/j.tecto.2015.10.008.

483 Mondol, N. H., Fawad, M., Jahren, J. and Bjørlykke, K.,, 2008. Synthetic mudstone
484   compaction trends and their use in pore pressure prediction. First Break,
485   26, 43-51.

486 Okino, K. and Fujioka, K., 2003. Central basin spreading center, Philippine Sea:
487   Structure of an extinct spreading center and implications for marginal basin
488   information. J. Geophys. Res. 108, 2040, doi:10.1029/2001JB001095.

489 Okino, Y., Shimakawa, Y. and Nagaoka, S., 1994. Evolution of the Shikoku Basin. J.
490   Geomag. Geoelect. 46, 463–479.

491 Parés, J. M., 2015. Sixty years of anisotropy of magnetic susceptibility in
492   deformed sedimentary rocks. Frontiers Earth Sci. 3, 1–13, doi:
493   10.3389/feart.2015.00004.

494 Potter, D. K. and Stephenson, A., 1988. Single-domain particles in rocks and
495   magnetic fabric analysis. Geophysical Research Letters, 15, 1097-1100, doi:
496   10.1029/GL015i010p01097.

497 Reagan, M. K., Ishizuka, O., Stern, R. J., Kelley, K. A., Ohara, Y., Blichert-Toft, J.,
498   Bloomer, S. H., Cash, J., Fryer, P., Hanan, B. B., Hickey-Vargas, R., Ishii, T.,
499   Kimura, J. I., Peate, D. W., Rowe, M. C. and Woods, M., 2010. Fore-arc basalts
500   and subduction initiation in the Izu-Bonin-Mariana system. Geochem.
501   Geophys. Geosys., 11, 1–17, doi: 10.1029/2009GC002871.

502 Reynolds, S. and Gorsline, D.S., 1992. Clay microfabrics of deep sea mud(stones),
503   California Continental Borderland. J. Sed. Petr. 62, 41-53.

504 Rochette, P., Jackson, M. and Aubourg, C., 1992. Rock Magnetism and the
505   interpretation of magnetic susceptibility. Reviews Geophys. 30, 209–226.

506 Sagnotti, L. and Speranza, F., 1993. Magnetic fabric analysis of the Plio-
507   Pleistocene clayey units of the Sant'Arcangelo basin, southern Italy. Physics
508   of the Earth and Planetary Interiors, 77, 165-176.

509 Sagnotti, L., Speranza, F., Winkler, A., Mattei, M. and Funiciello, R., 1998. Magnetic
510   fabric of clay sediments from the external northern Apennines (Italy). Phys.
511   Earth Planet. Int. 105, 73–93, doi: 10.1016/S0031-9201(97)00071-X.

512 Schwehr, K., Tauxe, L., Driscoll, N. and Lee, H., 2006. Detecting compaction
513   disequilibrium with anisotropy of magnetic susceptibility. Geochem.
514   Geophys. Geosys. 7, doi: 10.1029/2006GC001378.

515 Schlater, J. G. and Christie, P. A. F., 1980. Continental stretching: an explanation of
516   the post-mid-Cretaceous subsidence of the Central North Sea basin. Journal
517   of Geophysical Research, 85, 3711-3739.

518 Tarling, D. and Hrouda, F. (Eds.), 1993. Magnetic anisotropy of rocks. Springer
519   Science & Business Media.
520 Tauxe, L. and Kent, D. V., 2004. A simplified statistical model for the geomagnetic
521   field and the detection of shallow bias in paleomagnetic inclinations: was
522   the ancient magnetic field dipolar? Timescales Paleomag. Field, 145, 101–
523   115.
524 Terzaghi, K., 1925. Erdbaumechanik auf Bodenphysikalischer Grundlage. Franz
525   Deuticke, Liepzig-Vienna, 274 p.
526
527

528 **Figure captions**

529

530 Figure 1. (a) Location map of the Philippine Sea Plate (PSP) showing the main
531 geological structures and domains inferred from bathymetry, and the location of
532 IODP Site U1438. (b) Lithostratigraphic log from Site U1438. The grain size is
533 averaged over 5 m thick intervals. (cl) clay; (si) silt; (vfs-fs) very fine to fine sand;
534 (ms-vcs) medium to very coarse sand; (gr), granules. Unit subdivision is
535 indicated.

536

537 Figure 2. (a-c) Anisotropy of magnetic susceptibility results from 173 discrete
538 cubic samples from Unit I, IODP Hole U1438B, showing the variation with depth
539 of (a) the corrected anisotropy degree, P_J (b) the shape parameter, T, and (c)
540 mean susceptibility. (d-g) Variation with depth of physical property and
541 lithostratigraphic data from IODP Expedition 351 shipboard measurements
542 (Arculus et al., 2015a). (d) Density and porosity data from discrete samples. (e)
543 Age model based on magnetostratigraphy. Each point on the age-depth curve
544 represents a reversal of the magnetic polarity in the core dated using the
545 reference geomagnetic polarity time scale (GPTS). Sedimentation rates are
546 calculated on the basis of the magnetostratigraphy. (f) Simplified
547 lithostratigraphic log of Unit I. (g) Proxy for quartz content derived from peak
548 intensities on X-Ray diffraction spectra (note arbitrary units). The two dotted
549 gray lines bracket the interval in which anisotropy and physical parameters
550 progressively change (here defined as the 'initial compaction window').

551

552 Figure 3. Stereographic equal area projections of the principal susceptibility axes
553 from samples (a) above and (b) below 83 mbsf.

554

555 Figure 4. (a) High-temperature variation of low-field magnetic susceptibility
556 during a complete heating-cooling cycle, showing a clear Curie temperature of
557 ~580°C (heating curve). The cooling curve shows a slightly higher Curie
558 temperature probably due to the oxidation of original magnetite to maghemite.
559 (b) Isothermal remanent magnetization (IRM) acquisition curve from a
560 representative sample showing presence of low coercivity magnetite. (c)
561 Susceptibility vs. intensity of natural remanent magnetization (NRM) showing a
562 linear relationship suggesting constancy of ferromagnetic mineralogy downhole.

563

564 Figure 5. Variation with depth of (a) inclination and (b) declination of the
565 magnetic remanence in Unit I after alternating field (AF) demagnetization at 25

566 mT of archive half core sections (2 cm measurement interval; see Arculus et al.
567 (2015b) for full description of methodology). Data are in geographic coordinates,
568 after correction using FlexIT core orientation tool data. Declination and
569 inclination vary downward due to the reversals of the geomagnetic field. (a)
570 Inclination decreases significantly below core 9H (the effect is more visible in the
571 normally magnetized intervals). (b) Declination varies within each core likely
572 due to drilling-induced shear effects, particularly evident in cores 3H, 5H, 8H,
573 and 13H. The shear effect is expected to be minimum at the bottom of each core.
574 (c) Core distribution with depth from Hole U1438B.
575
576 Figure 6. Representative orthogonal vector plots of demagnetization data from
577 intervals used for the calculation of the mean inclination. We select only those
578 intervals in which 25 mT AF steps provide a reliable measure of the isolated
579 characteristic remanent magnetization directions (i.e., declination and
580 inclination of the 25 mT step is at an angle < 10° from the best fit line calculated
581 using the 20-40 mT interval). Black (white) dots represent the declination
582 (inclination) projection.
583
584 Figure 7. Variation of uniaxial vertical shortening derived from the density data
585 of Figure 2d (open circles) compared to published theoretical compaction trends
586 for clays and claystones. The two dotted gray lines bracket the interval in which
587 anisotropy and physical parameters progressively change (here defined as the
588 'initial compaction window').
589
590 Table S1. Summary of anisotropy of magnetic susceptibility data from Unit I of
591 IODP Hole U1438B.
592

Figure 2
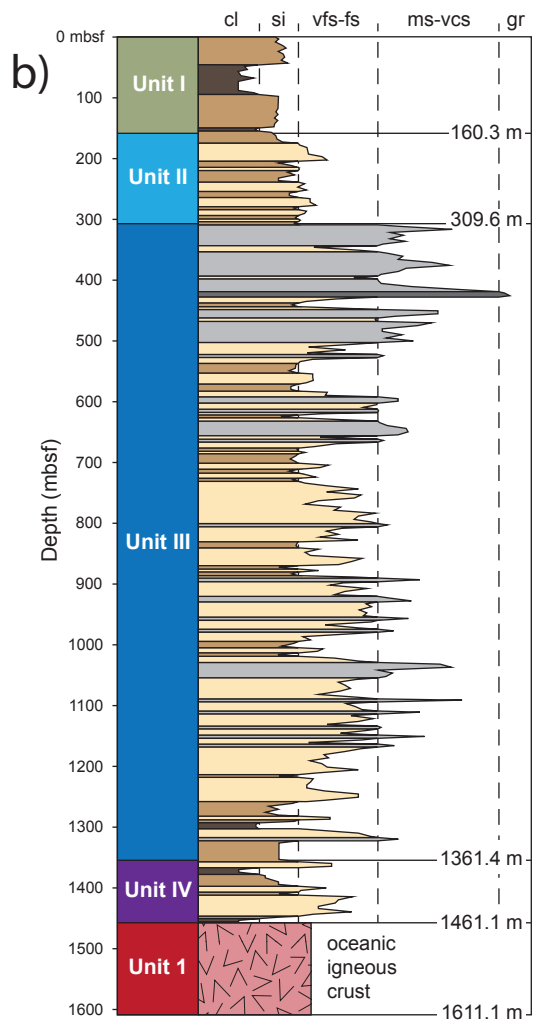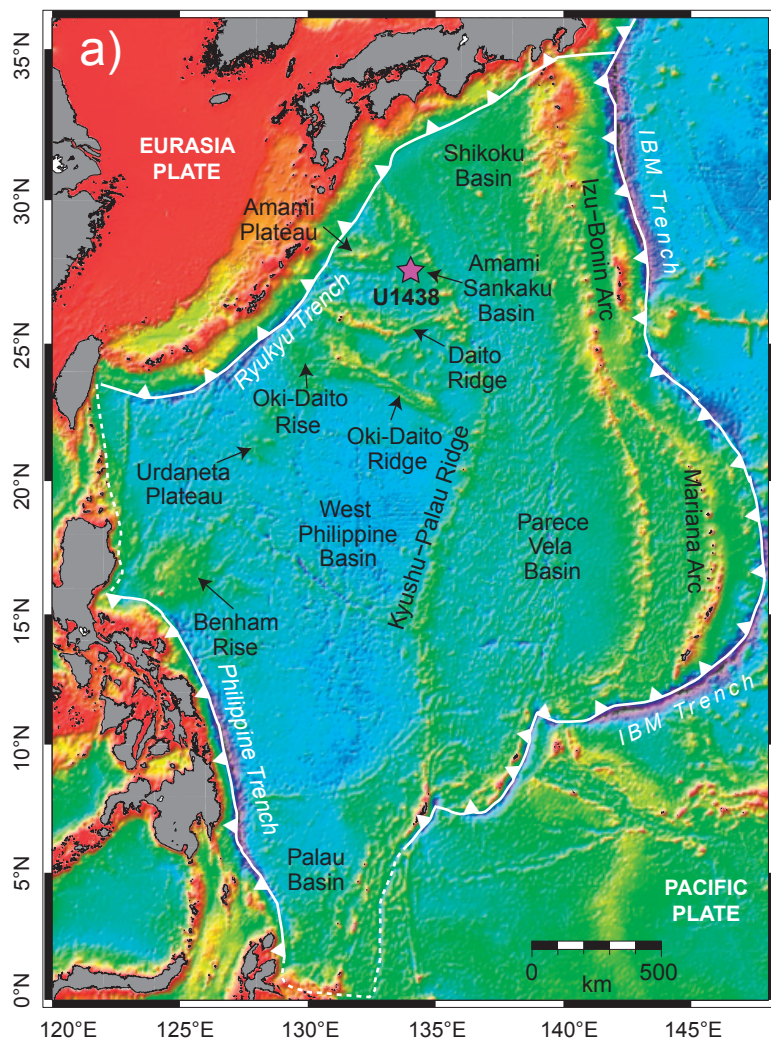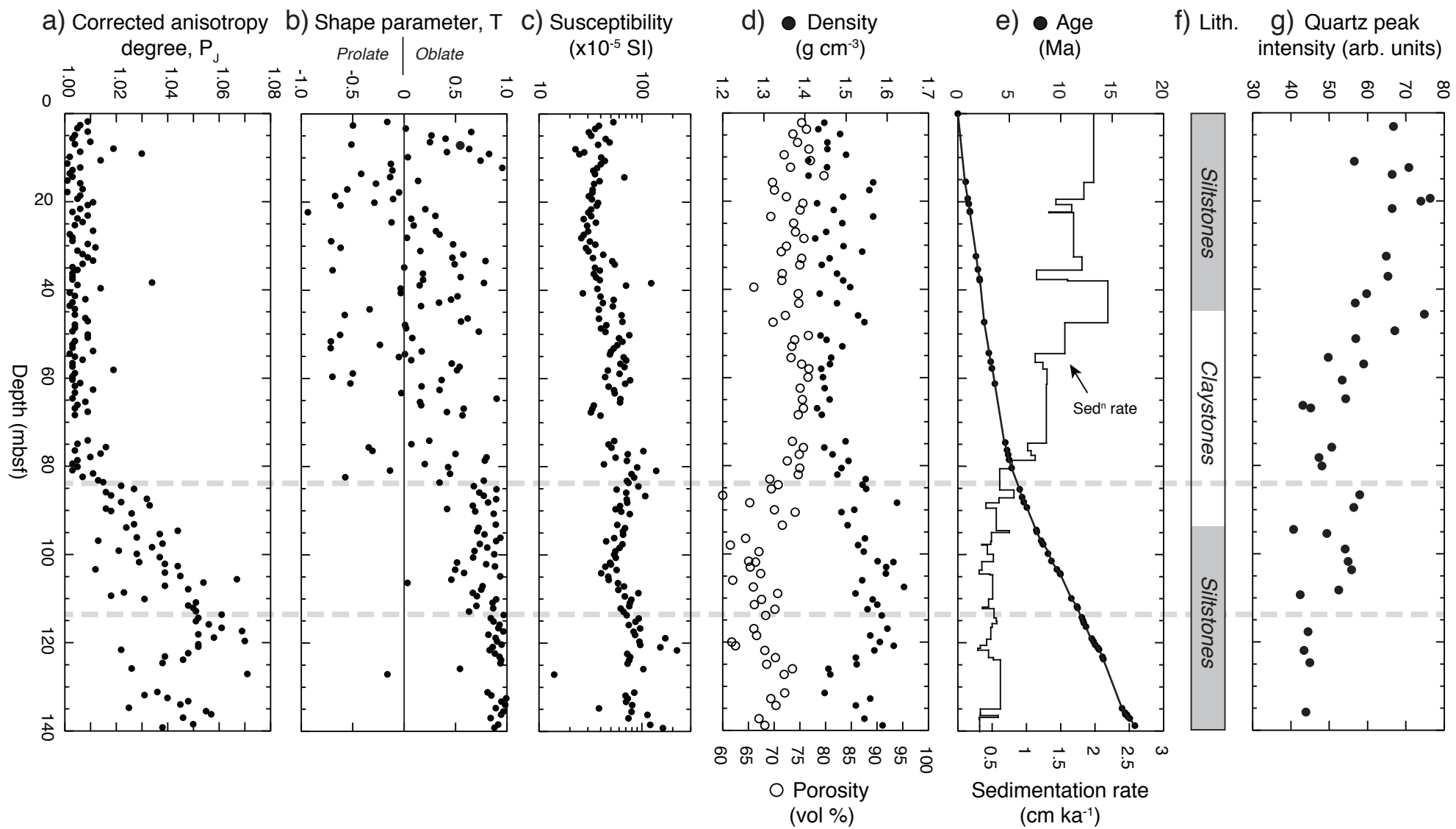
a) < 83 mbsf   N

b) > 83 mbsf   N

k_{max} k_{int} k_{min}

a)

Susceptibility (x 10^{-5} SI)

351-U1438B
7H5, 41 cm

Temperature (°C)

b)

$F = J/J_{max}$

$J_{max} = 10.3$ Am^{-1}

$\Delta F/\Delta F_{max}$

351-U1438B
7H5, 41 cm

Applied field (mT)

c)

NRM intensity (Am^{-1})

Susceptibility (x 10^{-5} SI)
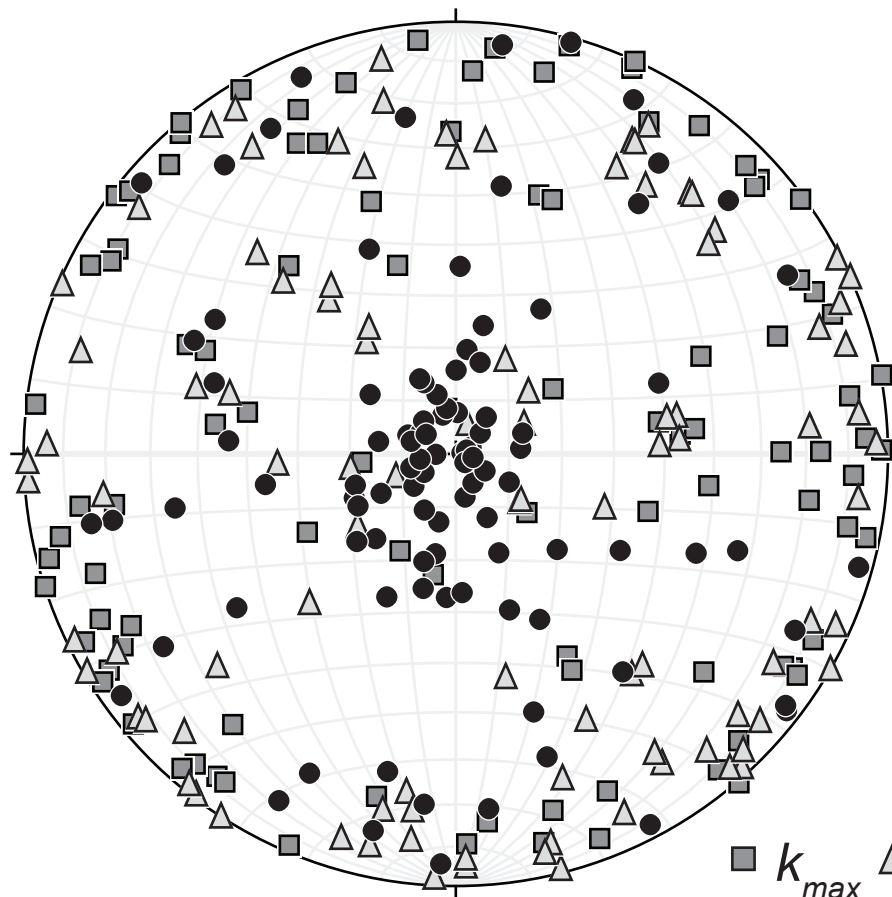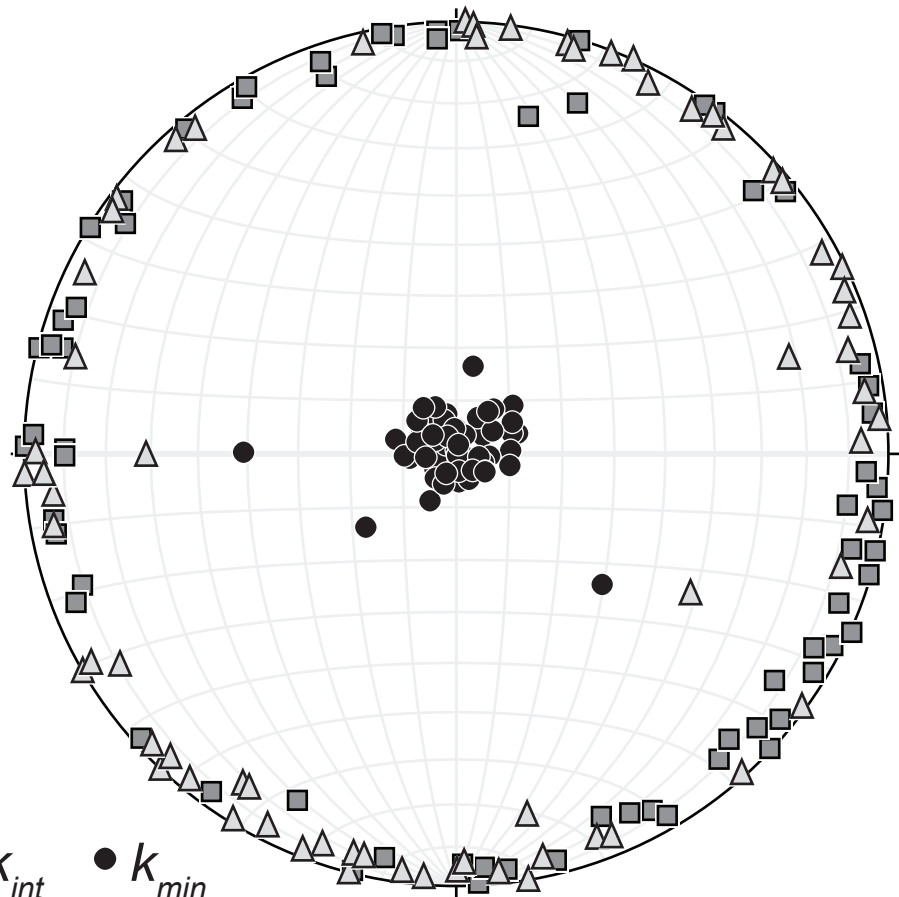
Figure 5
Click here to download Figure: Figure_5_Dec-Inc_plot.pdf
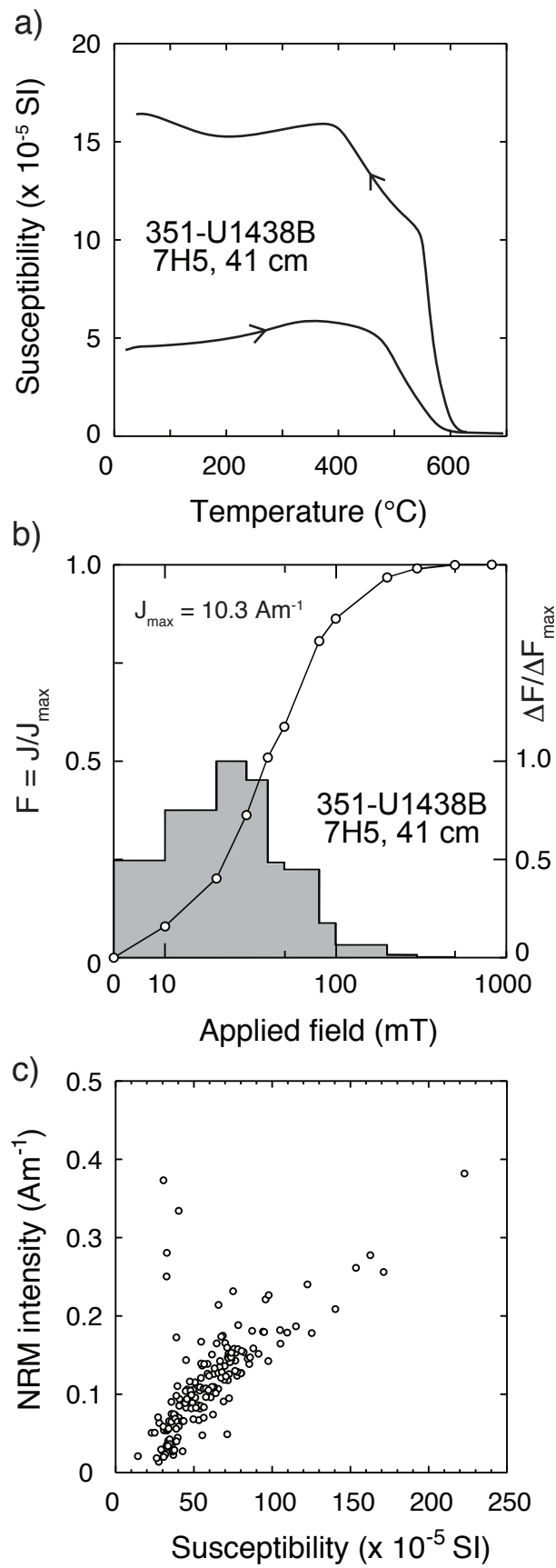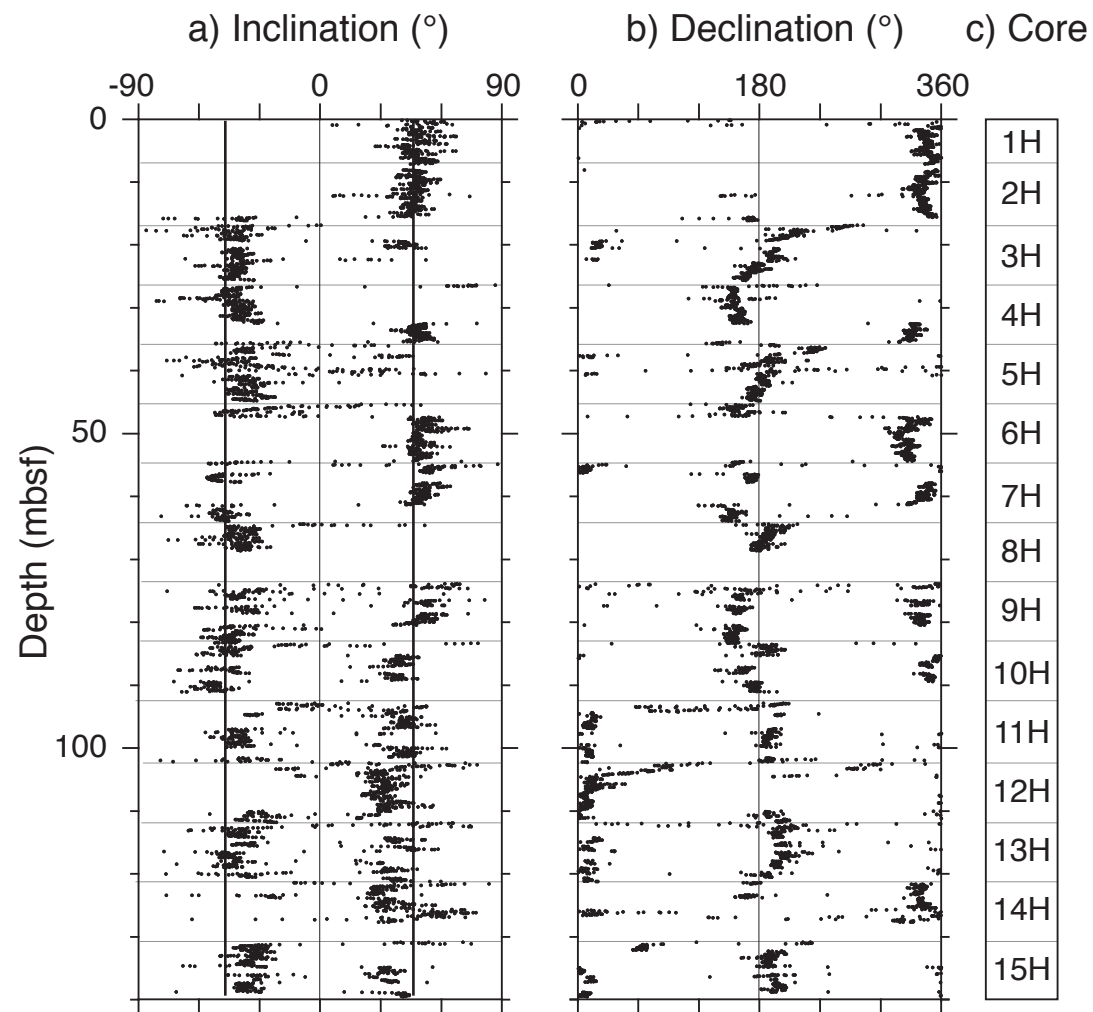
Figure 6
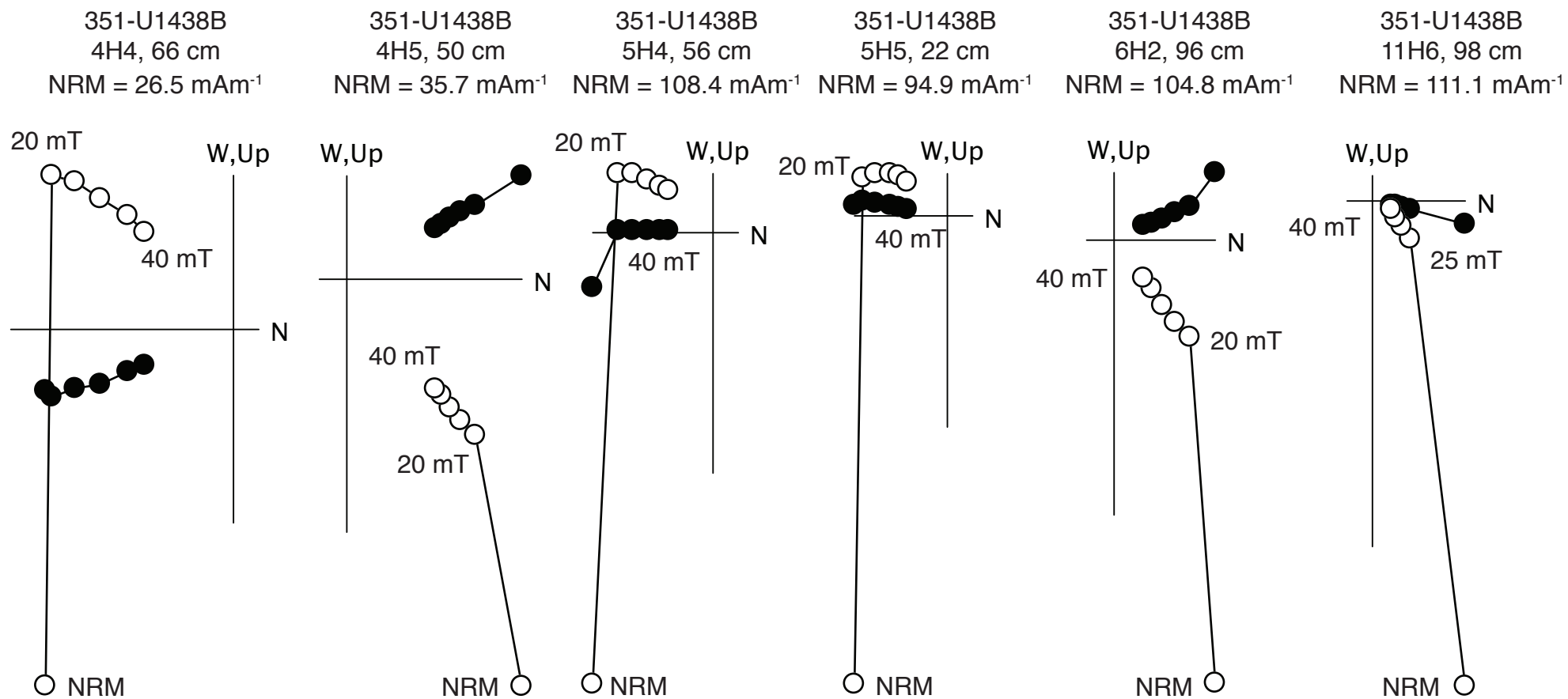[Click here to download Figure: Figure_6_Z-plots.pdf](#)

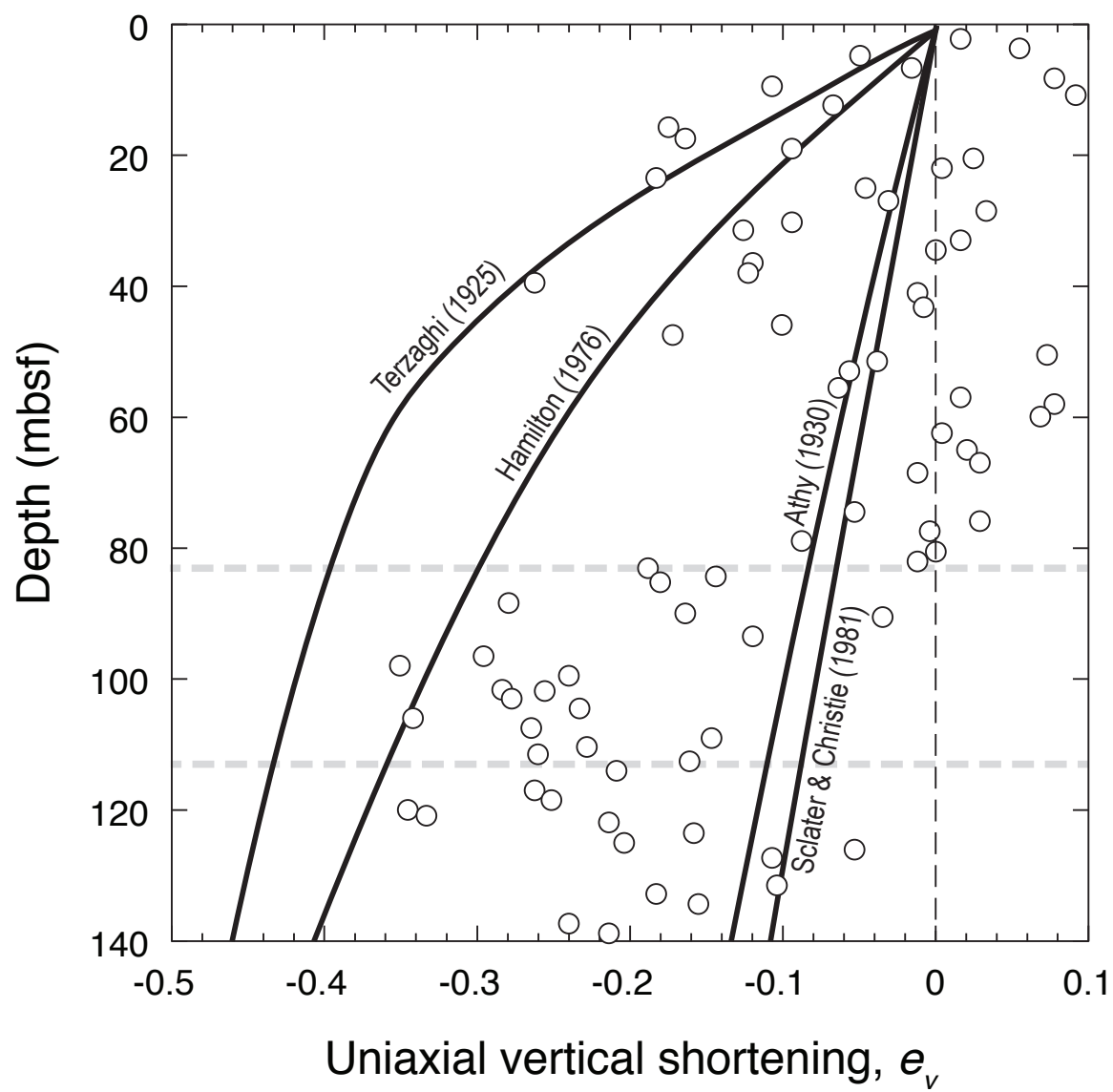351-U1438B
4H4, 66 cm
NRM = 26.5 mAm^{-1}

351-U1438B
4H5, 50 cm
NRM = 35.7 mAm^{-1}

351-U1438B
5H4, 56 cm
NRM = 108.4 mAm^{-1}

351-U1438B
5H5, 22 cm
NRM = 94.9 mAm^{-1}

351-U1438B
6H2, 96 cm
NRM = 104.8 mAm^{-1}

351-U1438B
11H6, 98 cm
NRM = 111.1 mAm^{-1}

Supplementary material for online publication only